A computational investigation of inviscid hypervelocity flow of a dissociating gas past a cone at incidence

By M. N. MACROSSAN[1] AND D. I. PULLIN[2]

[1] Department of Mechanical Engineering, University of Queensland, St Lucia, Qld. 4072, Australia

[2] Graduate Aeronautical Laboratories 105–50, California Institute of Technology, Pasadena CA 91125, USA

Calculations have been performed for the inviscid hypervelocity flow of nitrogen past a 15° semi-angle sharp cone at an incidence of 30°, at an enthalpy sufficiently high to produce dissociation/recombination chemistry downstream of the bow shock wave. A spatially second-order-accurate scheme for the numerical solution of the inviscid Euler equations was used combined with the Lighthill–Freeman model of the non-equilibrium ideal dissociating gas. The computational method has been used as a 'numerical wind tunnel' in order to gain understanding of the interaction between the gas dynamics and the finite-rate gas chemistry. Inviscid flow has been considered to ensure that the only physical lengthscales in the flow are those associated with the chemical reactions. It was found that a chemical lengthscale L_s based on the local dissociation length behind the shock on the windward plane of symmetry is an important governing parameter of the flow. However, as the flow lengthscale becomes large and the flow approaches the limiting case of equilibrium chemistry, L_s is not the dominant chemical lengthscale. This is particularly true of the leeward flow, which contains a shock–vortex structure. A simple modelling technique has been used to determine a more appropriate lengthscale, $L_{r,l}$, for the leeward flow as the equilibrium limit is approached. This lengthscale is based on the expected equilibrium conditions behind the cross-flow shock.

1. Introduction

There are now various proposals for the design and construction of hypersonic aerospace planes powered by air-breathing engines. The flight envelope into low Earth orbit will be very different from that of a rocket-powered vehicle and will include sustained periods of nearly level flight at velocities great enough to induce chemical dissociation and recombination of air in the external flow. The endothermic dissociation reaction will absorb a large portion of the stagnation enthalpy and this energy can be released in another part of the flow by the reverse, exothermic recombination reaction. During re-entry to the Earth's atmosphere at a high angle of attack the chemically active region will extend to the leeward body surface, changing the aerodynamics of the vehicle significantly. A comparison of timescales for finite-rate chemistry and gas flow past the body (Stalker 1989) indicates a range of possible aero-thermodynamic conditions from chemically frozen flow through a regime of non-equilibrium between the dissociation and recombination reactions, to equilibrium flow

where local chemical equilibrium can be achieved within each fluid particle in times much smaller than the time it takes the fluid to traverse the vehicle. These regimes of interaction between aerodynamics and gas chemistry are little understood for three-dimensional flows.

Here we study the hypervelocity flow about a sharp cone aligned at an angle of attack to the free-stream flow direction. This simple geometrical configuration gives rise to a complex flow containing vortices in the leeward flow. While it is certain that the fluid viscosity will have a profound effect on the leeward vortex system via a shock–boundary layer interaction, it is our purpose here to study the interaction of chemical reactions in the fluid with the gas dynamics in the outer flow by means of a simple model. Hence we consider here only inviscid flow, leaving consideration of the effects of finite viscosity for later study.

The general structure of hypersonic inviscid flow about a cone at incidence has been demonstrated by the calculations of Marconi (1989) and is illustrated in figure 1. For a perfect gas with a constant ratio of specific heats γ (i.e. with all chemical reactions inactive or 'frozen'), the flow is conical. A bow shock is followed by weakly rotational flow in the shock layer adjacent to the windward cone surface. The gas expands rapidly on the leeward surface and then is compressed as it approaches the leeward plane of symmetry. For sufficiently large angle of attack at hypersonic Mach number the flow is supersonic on the leeward surface and a pair of cross-flow shocks is produced where the flow turns to become approximately parallel to the leeward plane of symmetry. The resulting large entropy gradient along the leeward side of these shocks generates sufficient vorticity to separate the flow from the cone surface, producing a complex flow structure containing one or more pairs of compact vortices. Marconi (1989) shows that, owing to entropy discontinuities present at the separation line, the separation must take the form of a vortex sheet embedded in a background rotational flow. In an appropriate conical projection, the separation streamline, for strictly inviscid flow, makes a finite angle with the cone surface. This shock–vortical structure would be modified by the presence of the boundary layer on the cone surface and, in that case, separation may occur closer to the windward side; but as we have said this will not be considered further here.

We have used a computational fluid dynamics method, the Equilibrium Flux Method or EFM (Pullin 1980), to calculate the chemically reacting flow and to investigate the scaling laws for the interaction of the dissociation reactions,

$$N_2 + N \Leftrightarrow 2N + N \qquad (1\,a)$$

and
$$N_2 + N_2 \Leftrightarrow 2N + N_2, \qquad (1\,b)$$
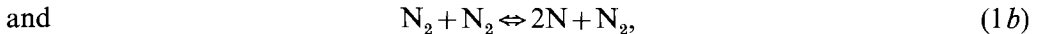
with the leeward vortical flow. Nitrogen is chosen as the 'test gas' because it allows us to study the interaction of aerodynamics and the simplest possible yet fundamentally important non-equilibrium chemical effects typical of high-enthalpy air flow.

Experiments on hypervelocity flow past bodies of revolution at incidence are being performed (Krek, Hannemann & Pullin 1989) in the T4 shock-tube wind tunnel ('shock tunnel') at the University of Queensland and in our calculations the range of free-stream conditions encompasses conditions typical of those that can be produced in the test section of the shock tunnel. We are interested in flows that can be produced in experimental facilities and have used the numerical method as a 'numerical wind tunnel'. We are not directly concerned with the question of how the results found in a typical high-enthalpy shock tunnel correspond to flight conditions in the atmosphere; this has been considered by Stalker (1989). However, there may be some limitations to the proposed scaling laws, which are based on the assumption that the recombination

reaction rate is negligible, an assumption that may not be justified because of the high density of the test flow (Macrossan 1990).

In earlier work Macrossan (1989, 1990) calculated the flow about a two-dimensional blunt body with non-equilibrium chemistry using a spatially first-order-accurate version of the numerical method, and preliminary results for three-dimensional cone flow (Macrossan, Pullin & Richter 1989) have been presented. A second-order version of EFM (Macrossan & Pullin 1990) is used here, in which linear gradients of flow properties are assumed across each cell in each direction of the three-dimensional computational grid. The gradients are taken equal to the one-sided gradient that has the smallest absolute value, or zero when the one-sided gradients differ in sign. This is the so-called *min-mod* technique (van Leer 1979; Yee 1989). The second-order version of EFM gives good resolution of the cross-flow shock and the shock-induced vortex system in the leeward flow.

In the following sections we describe the chemical model and the free-stream conditions used in our calculations. Then we identify the dimensional groups on which the computed flow depends. Next we give details of the computational grid and procedures, and test the computational method for a special case where our three-dimensional calculations should produce conically symmetric flow. Next the nature of the cone flow is discussed and the importance of a chemical lengthscale based on expected conditions behind the windward shock is shown. We then consider in more detail the flow behind the leeward cross-flow shock and show that it displays a complicated dependence on the windward chemical lengthscale. Finally, a dominant lengthscale for the leeward flow, based on the expected conditions behind the cross-flow shock, is determined from a simple numerical modelling technique.

2. Chemistry model

We use Lighthill's (1957) ideal dissociating gas with the appropriate chemical-reaction-rate equation (Freeman 1958) to represent the chemical dynamics of nitrogen. The law of mass action, which relates the chemical composition to the temperature and density at equilibrium, is

$$\alpha^2/(1-\alpha) = \rho_d/\rho \exp{(-\theta_d/T)}, \tag{2}$$

where
$$\alpha = [\mathrm{N}]/([\mathrm{N}]+2[\mathrm{N_2}]) \tag{3}$$

is the mass fraction of dissociated nitrogen, T is the temperature of the mixture of N and $\mathrm{N_2}$, $\theta_d = 113200$ K is the dissociation temperature, and ρ_d, the characteristic density, is an approximation to a collection of terms in the partition functions for N and $\mathrm{N_2}$ which varies only slightly with temperature and is taken by Lighthill to be a constant, having a value of 130 gm cm^{-3}. The assumption that ρ_d is constant is equivalent to representing the sum of the equilibrium values of energy of electronic excitation of N and vibrational excitation of $\mathrm{N_2}$ by the energy of a single degree of freedom for $\mathrm{N_2}$ which is fully excited at all temperatures.

The equation of state for the mixture of N and $\mathrm{N_2}$ is

$$p = \rho(1+\alpha)RT, \tag{4}$$

where p is pressure and R is the ordinary gas constant for $\mathrm{N_2}$. The ratio of specific heats γ for the ideal dissociating gas, assuming the composition α is fixed, is given by

$$\gamma = \tfrac{1}{3}(4+\alpha) \tag{5}$$

and the enthalpy is given by
$$h = R[\alpha\theta_d+(4+\alpha)T]. \tag{6}$$

The net production rate of N can be expressed as the difference between the total dissociation rate $(d\alpha/dt)_d$ and the total recombination rate $(d\alpha/dt)_r$. Thus

$$d\alpha/dt = (d\alpha/dt)_d - (d\alpha/dt)_r, \tag{7}$$

where

$$(d\alpha/dt)_d = \rho C(\alpha, T)(1-\alpha)\exp(-\theta_d/T), \tag{8}$$

$$(d\alpha/dt)_r = \rho^2 C(\alpha, T)\alpha^2/\rho_d \tag{9}$$

and

$$C(\alpha, T) = [2C_1 T^{\eta_1}\alpha + C_2 T^{\eta_2}(1-\alpha)]/W, \tag{10}$$

where W is the molar mass (molecular weight) of N_2 and C_1, C_2, η_1 and η_2 are constants. Note that $C(\alpha, T)$ takes account of the different third-body efficiencies in (1a) and (1b). We have used the values $C_1 = 8.5 \times 10^{25}$ (c.g.s. units), $\eta_1 = -2.5$ for N as the third body, and $C_2 = 2.3 \times 10^{29}$ (c.g.s. units), $\eta_2 = -3.5$ for N_2 as the third body. These values were found experimentally by Kewley & Hornung (1974).

3. Free-stream conditions

The free-stream conditions used for the numerical simulations reported here are shown in table 1. Two values of flow energy and two values of flow density have been used to give four sets of free-stream conditions. In the two high-energy conditions the stagnation enthalpy,

$$H_0 = \tfrac{1}{2}u_\infty^2 + R[\alpha_\infty \theta_d + (4 + \alpha_\infty) T_\infty], \tag{11}$$

is approximately 28 MJ kg^{-1} and these conditions are labelled H28 and L28. For the two low-energy flows, labelled H22 and L22, H_0 is approximately 22 MJ kg^{-1}. The free-stream density for conditions L28 and L22 is approximately equal to the density of the Earth's atmosphere at an altitude of 50 km while for H28 and H22 the density is an order of magnitude larger and is typical of the density obtained in the T4 shock tunnel. We have made

$$M_\infty = u_\infty/[\tfrac{1}{3}(4 + \alpha_\infty)(1 + \alpha_\infty) RT_\infty]^{\frac{1}{2}}, \tag{12}$$

which is the Mach number based on the speed of sound in the free stream (for frozen chemistry), approximately 5 in each case.

We have taken the free-stream flow to be in chemical equilibrium, which is not true of laboratory-produced flows. The rapid expansion of the test gas in the nozzle of a shock tunnel will produce a test flow that is about 10% dissociated. However, earlier work (Macrossan 1990) has shown that the typical test flows, at least for a blunted flat plate at an angle of attack, are not greatly different from those that would be produced if the free stream were in chemical equilibrium with a low degree of dissociation.

Except for the test cases discussed in §5, all calculations were performed with a cone semi-angle $\theta = 15°$ and an angle of attack $\delta = 30°$.

4. Chemical effects (scaling)

We have eliminated the effects of many possible flow parameters by investigating the simple case of inviscid flow, a fixed chemical model and a free-stream flow in chemical equilibrium. Further simplification is achieved by considering a circular cone with a fixed cone semi-angle θ with its axis at a constant angle of attack δ to the free-stream velocity. Let ϕ denote the azimuthal angle from the windward plane of symmetry and let the origin of x-axis be at the cone tip and its direction be along the body axis, as shown in figure 1. We expect that some flow property such as the surface pressure p_s will display a functional dependence such as

$$p_s/p_\infty = \mathscr{F}(\phi, x/L_1, x/L_2, \rho_\infty/\rho_d, u_\infty^2/(R\theta_d), T_\infty/\theta_d), \tag{13}$$
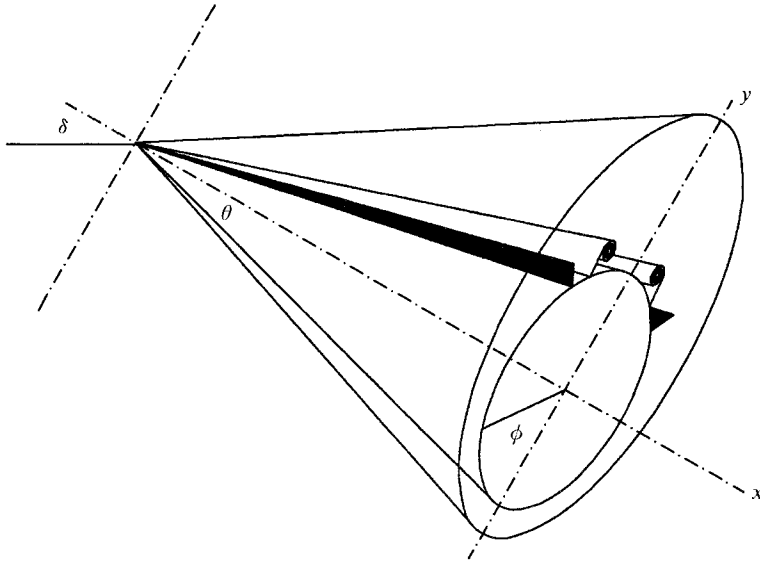
FIGURE 1. Conical flow of an inviscid gas about a cone flying at an angle of attack
(after Marconi 1989).

	H28	L28	H22	L22
Velocity u_∞ (km s^{-1})	6.696	6.541	5.954	5.912
Density ρ_∞ (10^{-3} kg m^{-3})	9.974	1.000	9.998	1.000
Temperature T_∞ (K)	4469.0	4232.0	3581.3	3534.9
Dissociation† α_∞	0.0113	0.0176	0.000493	0.00126
Stag. enthalpy H_0 (MJ kg^{-1})	28.12	27.03	21.99	21.18
Mach number‡ M_∞	5.000	5.000	5.000	4.995
Chemical length‖ L_s (m)	0.020	0.248	0.075	0.827

Notes:
  † Value is at chemical equilibrium.
  ‡ Based on the 'frozen' speed of sound, see (12).
  ‖ Reaction length behind windward oblique shock, (19).

TABLE 1. Free-stream conditions

where
$$L_1 = u_\infty W/(\rho_d C_1 \theta_d^{\eta_1}) \qquad (14)$$

and
$$L_2 = u_\infty W/(\rho_d C_2 \theta_d^{\eta_2}) \qquad (15)$$

are the chemical lengthscales associated with the two possible collision partners in (1). Notice that M_∞ and α_∞ do not appear directly in the list of arguments since if ρ_∞, T_∞ and u_∞ are given the condition of chemical equilibrium in the free stream, (2), is sufficient to determine both these properties.

In the double limit x/L_1 and $x/L_2 \to 0$, the flow is chemically frozen and the flow state does not depend on x. Because of the symmetry of the conical body the flow is conically symmetric in this limit. At the opposite extreme, when x/L_1 and $x/L_2 \to \infty$ the flow is again independent of x and is again conically symmetric. For finite and non-zero values of x/L_1 and x/L_2 the flow is not conically symmetric. One aim of the present study is to search for a single chemical lengthscale which combines the effects of not only L_1 and L_2 but all the parameters in (13) to which the flow is sensitive.

Other measures have been used to characterize the flows. A non-dimensional measure, χ, of the vortex size at a distance x from the cone tip should be some function of the free-stream conditions such as

$$\chi = \mathscr{G}(x/L_1, x/L_2, \rho_\infty/\rho_d, u_\infty^2/(R\theta_d), T_\infty/\theta_d). \tag{16}$$

We also consider the integrated surface pressure force, or rather the corresponding pitching moment coefficient,

$$C_z = M_z/(\tfrac{1}{2}\rho_\infty u_\infty^2 \, xA_x), \tag{17}$$

where M_z is the magnitude of the pitching moment (about the z-axis through the cone tip) which acts on that portion of the cone up to the distance x. $A_x = \pi(x\tan\theta)^2$ is the cross-sectional area of the cone at station x. We expect that this coefficient should be a function of the free-stream conditions as follows:

$$C_z = \mathscr{K}(x/L_1, x/L_2, \rho_\infty/\rho_d, u_\infty^2/(R\theta_d), T_\infty/\theta_d). \tag{18}$$

5. Body and grid geometry, details of computations

Because of the flow symmetry about the (x, y)-plane, only one half of the flow ($z > 0$) was considered. A body-fitted grid of $N_1 \times N_2 \times N_3$ cells was used, where N_1 is the number of cells along the body (the x-direction), N_2 is the number normal to the body surface and N_3 is the number between the windward and leeward planes of symmetry in the azimuthal direction. The cells were concentrated near the cone surface and near the leeward plane of symmetry. The cell size in the x (or N_1)-direction varied in order to keep the cell width an approximately constant fraction (0.06) of the local cone radius.

It was not possible to resolve the starting flow at the cone tip to the same accuracy as the flow downstream. An initial calculation for a short cone was performed with a grid of $N_1 \times N_2 \times N_3 = 5 \times 24 \times 50$. A 'time-marching' mode of EFM was used in this initial grid in which the conservation equations were integrated forward in time, in steps of Δt, from impulsive initial conditions until steady state was reached. The downstream conditions from this grid were then transferred to a new grid which extended far downstream. In this grid the numbers of cells in the cross-flow directions were $N_2 = 48$ and $N_3 = 100$ and a 'space-marching' mode of EFM was used. In this mode steady state was found on successive slices (sub-grids) using the upstream conditions found previously in the calculations. The moving space-marching sub-grid was two cells wide in the marching direction and was stepped downstream one cell at a time, so that only the conditions in the upstream cell were saved at each step. The ratio of the time step Δt to the smallest fluid or wave transit time across any cell, for both time-marching and space-marching, was kept in the range 0.6–0.7 for all calculations reported here.

Space-marching can only be successful if the flow is everywhere supersonic and it is best if the gradients in the marching direction are small, as is true for the cone flow. For chemically active flow the space-marching was continued to large distances downstream. As a matter of convenience this was done in a series of separate runs, each of which marched the solution about thirteen steps downstream and required a CPU time between 15 and 22 hours on an IBM RISC 6000/530 workstation.

As a test of EFM we consider some results for a fully three-dimensional calculation in which the chemical composition was frozen. In this case our three-dimensional calculations should yield a conical flow. The effective γ was 1.4, the free-stream Mach number was $M_\infty = 5$, the cone semi-angle was $\theta = 10°$ and the angle of attack was $\delta = 20°$, conditions that correspond to those in the calculations of Marconi (1989)

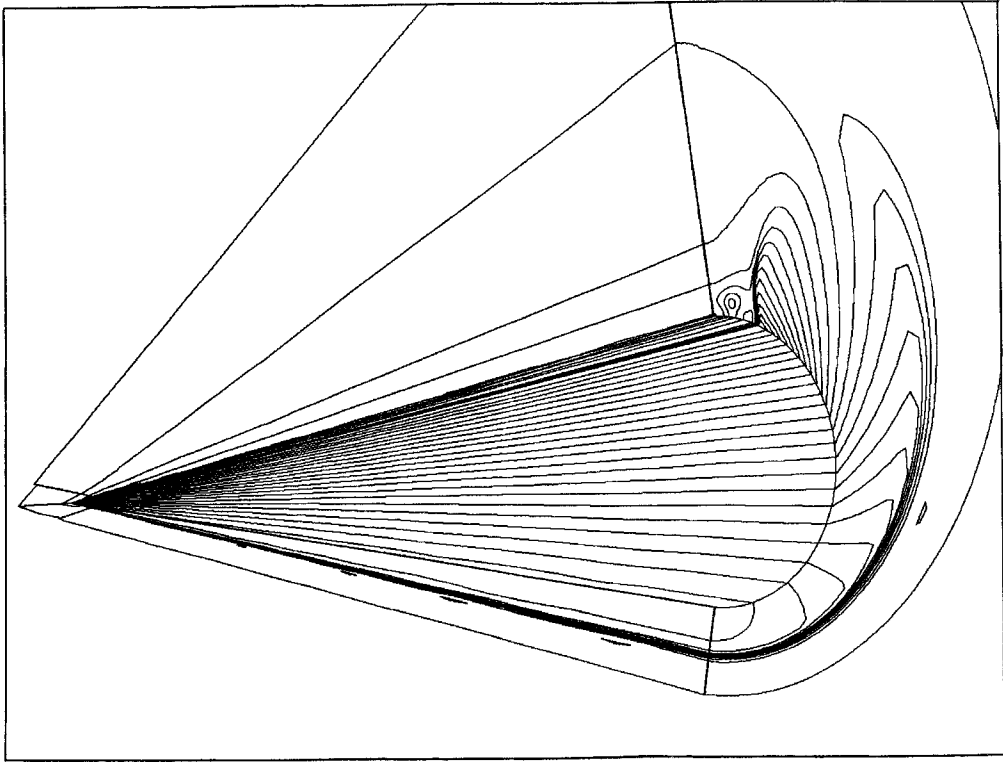FIGURE 2. Contours of log (p/p_∞) as calculated by EFM for perfect gas flow with $M_\infty = 5$, $\theta = 10°$, $\delta = 20°$. Grid size; $3 \times 24 \times 50$, $22 \times 48 \times 100$. Contours are shown on the cone surface, the windward and leeward planes of symmetry and a surface roughly normal to the rear surface of the cone.

who used a numerical method specialized for the conical flow of a perfect gas. Figure 2 shows some typical EFM results and, as expected, the flow state is conically symmetric (except very near the cone tip), that is the state is constant along any ray emanating from the tip of the cone. Figure 3 shows a detailed view, looking along the axis of the cone, of the conically projected stream surfaces where they roll up to form a vortex near the leeward plane of symmetry. The cone surface appears as a circular arc. The image was constructed from the data in a cross-flow section of the space-marching grid after 24 steps in the x-direction. This vortex is very similar to that found by Marconi (1989).

Figure 4 shows, for the same test calculation, the surface pressures, as calculated by us and Marconi, on the leeward surface of the cone in the vicinity of the leeward plane of symmetry. The EFM results are for two different grid resolutions; in both cases the time-marching grid $(N_1 \times N_2 \times N_3)$ at the nose was $5 \times 24 \times 50$, whereas the space-marching grid was 24×50 in the cross-flow direction $(N_2 \times N_3)$ in one case and 48×100 in the other. Marconi's calculation method employed a shock-fitting procedure to determine the position of the leeward cross-flow shock and hence his results show the shock as a discontinuity, whereas EFM produces a shock smeared over a few cells. Limitations of computational power prevented us from investigating the effects of a more refined grid in the cross-flow directions but, if we take Marconi's results (which were obtained on a somewhat finer computational grid) as the 'exact' solution, it is clear from figure 4 that any grid-dependent effects in the EFM fluid-flux calculations are small, outside the smeared shock, for our most refined grid.
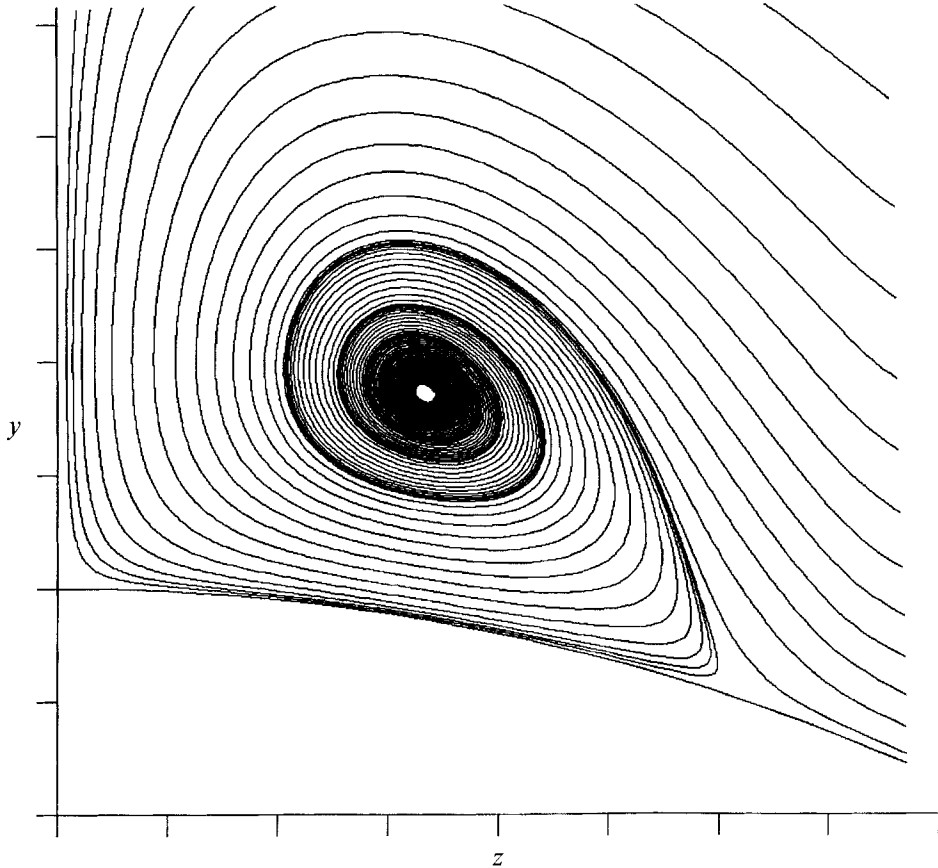
FIGURE 3. Conical projection of cross-flow streamlines near the leeward plane of symmetry.
Perfect gas, conditions as for figure 2.

6. Chemically reacting flow

Hornung (1972) found by considering calculated shock stand-off distances ahead of a sphere in hypervelocity flow of nitrogen, that a characteristic reaction length immediately behind the normal shock was an important governing parameter and his experimental results confirmed this (see also Macrossan 1990). For the flow being considered here, the equivalent reaction rate is that behind the oblique shock attached to the tip of the sharp cone. Therefore the characteristic reaction length in the shock layer may be taken as

$$L_s = u_\infty/(\mathrm{d}\alpha/\mathrm{d}t)_s, \tag{19}$$

where $(\mathrm{d}\alpha/\mathrm{d}t)_s$ is evaluated from (7)–(10) for the density, temperature and composition behind an oblique shock (with the chemical reaction frozen across it). We have assumed that the characteristic windward shock is one inclined to the free-stream velocity at $\theta + \delta = 45°$, which is the sum the cone half-angle and the angle of attack. Since α_∞ is very small the net reaction rate $(\mathrm{d}\alpha/\mathrm{d}t)_s$ is virtually the same as the rate for the forward (dissociation) reaction alone but in fact we have not made this approximation when evaluating L_s.

Hornung (1972, 1976) showed that the two-dimensional flow behind a curved shock wave contained a region of intense reaction close to the shock followed by a large region of chemically frozen flow. The reaction region is localized because the forward (dissociation) reaction rate, (8), is an exponential function of temperature and there is
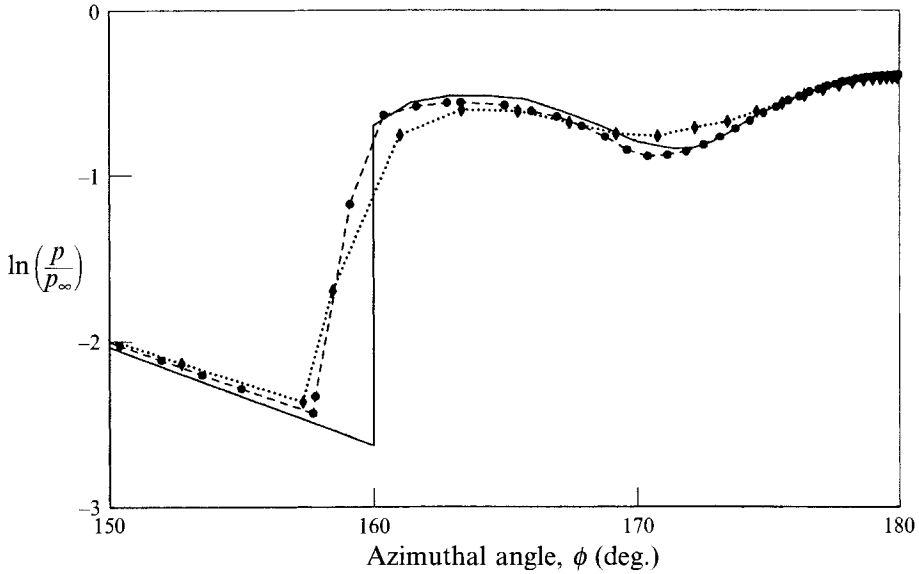
FIGURE 4. Cone surface pressure near the leeward plane of symmetry. Perfect gas, conditions as for figure 2. EFM, three-dimensional calculations: $\cdots\blacklozenge\cdots$, 24×50 ($N_2 \times N_3$) cross-flow grid; $\text{---}\bullet\text{---}$, 48×100 cross-flow grid. Conical 'shock fitting' method (Marconi 1989): ———, 89×89 grid.
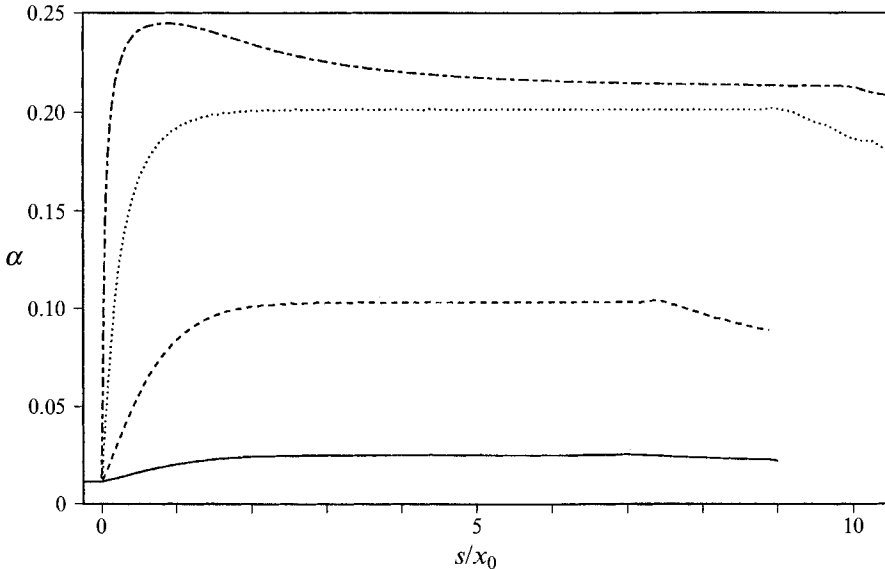

FIGURE 5. Dissociation fraction α along streamlines crossing the shock at x_0 and azimuthal location ϕ_0. Free-stream conditions H28 in table 1. $\theta = 15°$, $\delta = 30°$, ———, $x_0/L_s = 4.1 \times 10^{-3}$, $\phi_0 = 0.22$; ---, $x_0/L_s = 4.7 \times 10^{-2}$, $\phi_0 = 0.22$; ......, $x_0/L_s = 2.5 \times 10^{-1}$, $\phi_0 = 0.24$; $\text{---}\cdot\text{---}$, $x_0/L_s = 3.9$, $\phi_0 = 0.25$. L_s is given by (19).

a rapid fall in temperature which accompanies the endothermic dissociation reaction. Hornung (1988) and Stalker (1989) have used the term 'quenching' to distinguish this rapid reduction of the dissociation rate from the 'freezing' of the recombination reactions which is caused by a decrease in density and is a familiar phenomenon seen in the nozzle flow of test facilities.
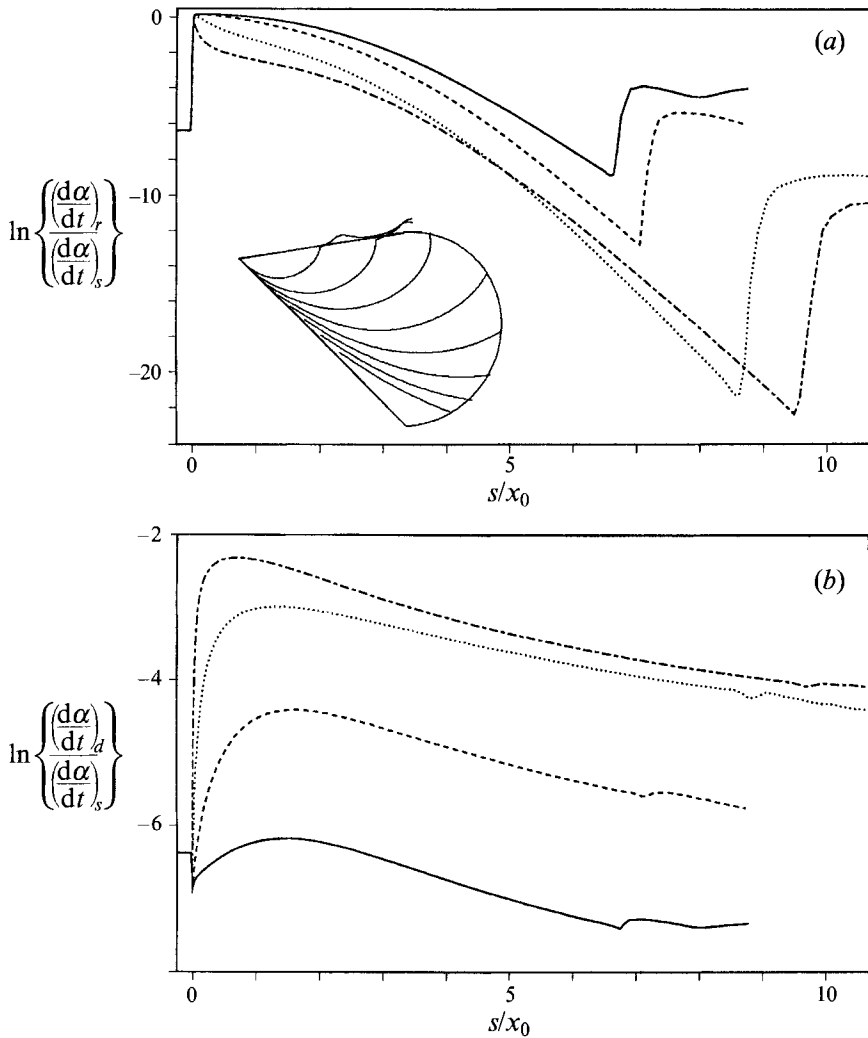
FIGURE 6. (*a*) Dissociation rate $(d\alpha/dt)_d$ of (8), and (*b*) recombination rate $(d\alpha/dt)_r$ of (9), along streamlines corresponding to those for figure 5. $(d\alpha/dt)_s$ as in (19).

Figure 5 shows the variation in chemical composition α, behind the windward shock, along some selected streamlines which cross the windward shock at an azimuthal angle $\phi_0 \approx 12°$ from the windward plane of symmetry but at different distances, x_0, from the cone tip. Figure 6 shows the variation in the dissociation and recombination rates of (8) and (9) along these same streamlines, as well as a pictorial view of some typical streamlines in the flow near the cone surface. The origin of s, the distance along the streamline, has been set where the streamline crosses the shock and the streamline has been followed until just after it crosses the leeward cross-flow shock. The streamline distance has been normalized as s/x_0 and the slightly different (normalized) lengths travelled between the windward and leeward shocks are an indication that the streamline patterns in the shock layer are different at different distances from the cone tip. The absolute distance travelled between these shocks, which is roughly proportional to the starting coordinate x_0, determines in general how far the dissociation reaction can proceed behind the shock and it can be seen in figure 5 that the dissociation after
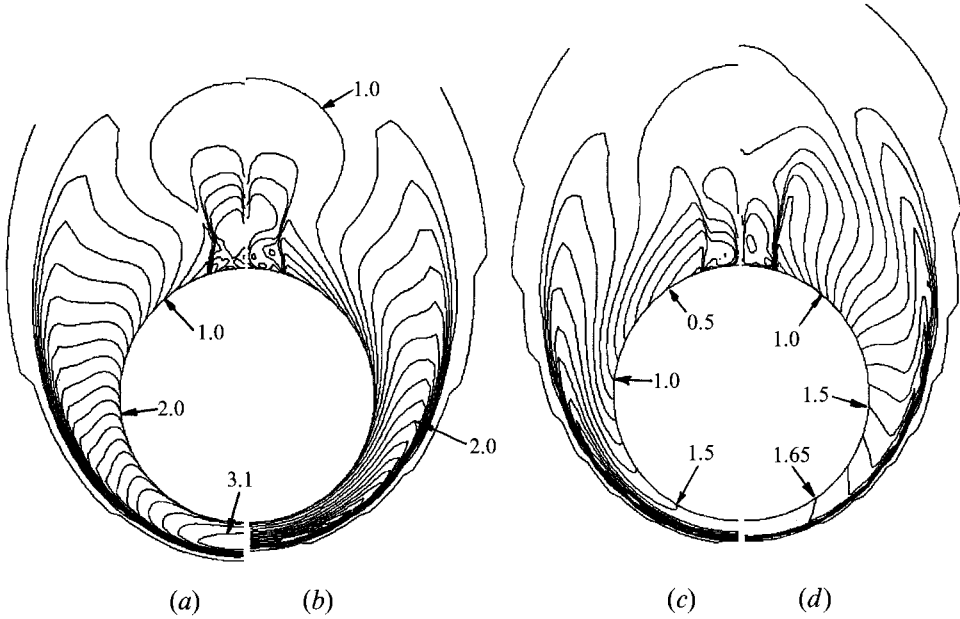
FIGURE 7. Temperature contours, T/T_∞, in a cross-section of the flow. Free-stream conditions H28, table 1. (a) $x/L_s = 0.03$, (b) $x/L_s = 0.89$, (c) $x/L_s = 18.8$, (d) $x/L_s = 1829$.

the shock rises to a different value in each case. There is some dissociation cooling associated with this rise and the amount of this dissociation cooling (which is proportional to the rise in α) increases at increasing distance from the cone tip. For the streamline starting furthest downstream, at $x_0/L_s \approx 3.9$, which crosses the leeward shock at $x_0/L_s \approx 39$, the rise in α and the consequent dissociation cooling is enough to reverse the reaction and bring about a fall in α. Closer to the cone tip the dissociation remains virtually constant along the streamline.

Superimposed on any dissociation cooling there is a fluid dynamic cooling associated with the expansion of the flow towards the leeward surface. This cooling, as opposed to the chemical cooling, will be virtually independent of the distance from the cone tip. Both types of cooling 'switch off' the reaction rate but an indication of which effect is dominant is given by the variation in reaction rates along the streamlines, which is shown in figure 6(a). In all cases the dissociation rate decreases by many orders of magnitude as the flow expands towards the leeward surface. However, for the streamlines beginning furthest downstream there is an even more rapid dissociation cooling immediately behind the shock. The first indication of this quenching effect, to use Hornung's term, can be seen on the streamline starting at $x_0/L_s \approx 0.38$ and we shall see later that at this value of x/L_s the influence of the chemical reactions on the flow is most pronounced. The quenching is even stronger at $x_0/L_s \approx 3.9$.

The recombination rates $(\mathrm{d}\alpha/\mathrm{d}t)_r$ are shown in figure 6(b). The recombination rate rises through the shock and, in each case, falls in the expansion around the body much less rapidly than the dissociation rate because it is less sensitive to temperature; see (8) and (9). By comparing the dissociation rate with the corresponding recombination rate, the regions of net dissociation and net recombination can be determined and it is found that the recombination region occupies a greater portion of the streamline as the distance downstream increases. At $x_0/L_s \approx 0.004$, recombination does not begin until $s/x_0 \approx 6$ and finishes at the leeward shock, while for $x_0/L_s \approx 0.047$ the recombination region begins closer to the windward shock, at $s/x_0 \approx 4.2$. In this case the dissociation
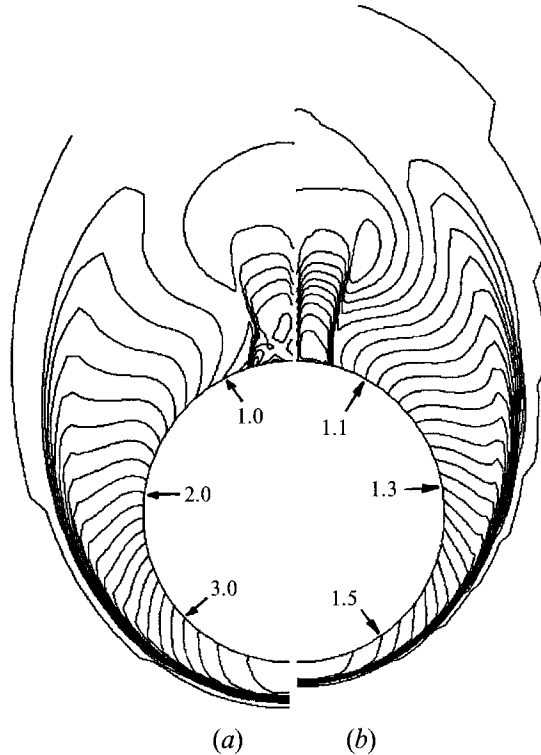
FIGURE 8. Temperature contours, T/T_∞, in a cross-section of the flow. Free-stream conditions H28, table 1. (a) Frozen chemistry, (b) equilibrium chemistry.

and recombination rates are virtually equal behind the leeward shock, that is, chemical equilibrium is established with some slight deviations either way at different points along the streamline. Further downstream, at $x_0/L_s \approx 0.38$ and 3.9 the recombination region begins at $s/x_0 \approx 2.5$ and 0.15 respectively.

It should be noted here that there is apparently some cross-streamline diffusion of chemical species immediately behind the leeward shock. This can be seen by the decrease in α behind the shock, which is not associated with any dramatic increase in the recombination rate behind the shock. This is a numerical error for a strictly Euler (diffusionless) flow but it must be emphasized that this diffusive decrease of α along the streamline does not involve a release of chemical energy into the flow. It does, however, involve a change, of less than 0.5% in the extreme, in the effective value of γ in the vortical flow behind the cross-flow shock.

Figure 7 shows the temperature contours on a cross-section of the grid at different distances x. Regions of rapid cooling, those where the contours are closely spaced, arise from the dissociating cooling effect and the regions of slower cooling arise from the expansion of the flow from the windward towards the leeward side of the cone. Close to the nose, at $x/L_s = 0.03$, some dissociation cooling of the flow behind the shock near the windward plane of symmetry can be seen and at greater azimuthal angles from the windward plane of symmetry there is conventional expansion cooling. There is a large temperature gradient near the cone surface. It appears that this thermal 'boundary layer' is made up of streamlines which have crossed the shock close to the windward plane of symmetry at slightly different angles and have undergone different amounts of dissociation cooling before being expanded around the surface.

For $x/L_s = 18.8$ the dissociation cooling region has contracted towards the shock and there is an expansion-cooled region near the body surface. At a great distance downstream, $x/L_s = 1829$, the dissociation cooling region is very thin and almost merged with the shock. The expansion cooling region extends over most of the flow and is very similar to that at $x/L_s = 0.03$ except for the absence of the thermal layer close to the surface and for the fact that the slow exothermic recombination reaction in the expansion region has reduced the rate at which the temperature decreases. It is noticeable that the azimuthal extent of the dissociation cooling region behind the shock increases as it contracts towards the shock.

It is instructive to compare the corresponding temperature fields for the frozen and equilibrium limits, which are shown in figure 8. The temperature gradients in the expansion are much smaller for the equilibrium flow, but the contour patterns are similar, particularly on the windward side of the cone and both differ from the contour patterns for non-equilibrium flow seen in figure 7. Notice that in the equilibrium calculations, the temperature never reaches the high value associated with frozen flow across the shock so there is no region of steep temperature gradient behind the shock. This is in accordance with what we would expect if the numerical method were able to resolve a discontinuous shock since such a shock would be followed by a discontinuity in temperature where the temperature would be reduced to the values appropriate to equilibrium conditions behind the shock.

The shock stand-off distance $\varDelta_s$ on the windward plane of symmetry was determined at various distances downstream. The shock location was taken at the point of maximum temperature gradient normal to the cone surface in the windward plane of symmetry. The results are shown in figure 9(a). Following Hornung (1972) the stand-off distance is normalized as $(\varDelta_s/x)\,(\rho_s/\rho_\infty)$, where ρ_s/ρ_∞ is the expected density ratio across the frozen oblique shock at an angle of $\theta+\delta$, but it happens that the density ratio is virtually the same for all our data. Data for the frozen and equilibrium limits have also been obtained and are shown in the figure at the minimum and maximum values of x. In the equilibrium limit, chemical equilibrium is enforced in each cell, after each flux calculation, while keeping the total energy in the cell constant. To obtain the frozen and equilibrium limiting values of $\varDelta_s/x$ a computation on a grid such as that for figure 2 was performed for which the total number of cells in the x-direction was considerably less than for the calculations for large x, there being no point in continuing to march downstream once the initial starting flow at the nose has settled down into a conical flow.

For chemically frozen flow the ratio $\varDelta_s/x$ is virtually the same for all sets of free-stream conditions, reflecting the fact that the Mach number and γ are almost the same in all cases. The onset of non-equilibrium is shown by the sudden decrease in the shock stand-off parameter at $x/L_s \approx 0.04$. The chemical length L_s is evidently a good correlation parameter up to $x/L_s \approx 2$ at which point the data for different stagnation enthalpies separate. For the low-energy data there is a further separation at $x/L_s \approx 10$ for the different densities, and the different limiting values are reached by $x/L_s \approx 200$. For the high-energy data, the separation according to density and the approach to the equilibrium limits are at slightly higher values of x/L_s (20 and 300 respectively).

In figure 9(b) we normalize the shock stand-off distance as

$$(\varDelta_s-\varDelta_e)/(\varDelta_f-\varDelta_e),$$

where $\varDelta_f$ and $\varDelta_e$ are the values found at the frozen and equilibrium limits respectively. While this normalization gives a reasonable overall correlation, the collapse of the data becomes slightly worse in the range $0.01 < x/L_s < 20$.
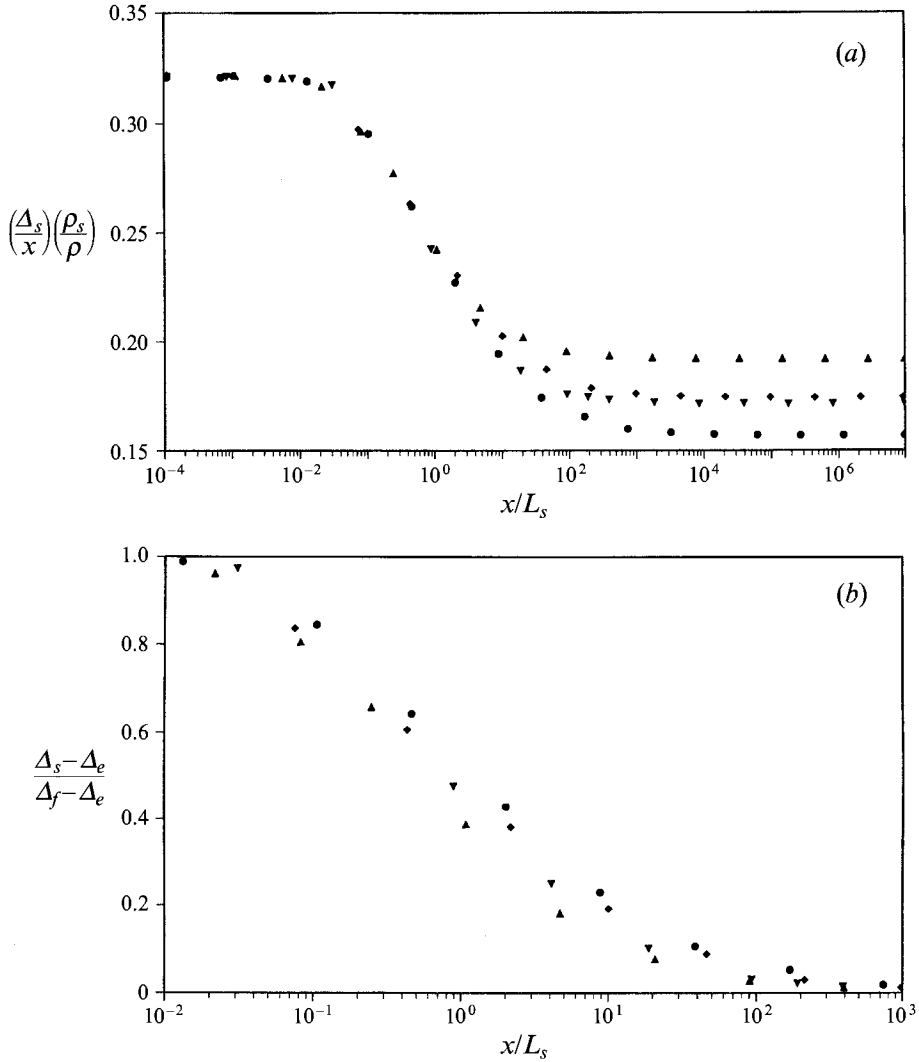
FIGURE 9. Shock stand-off distance $(\rho_s/\rho_\infty)(\varDelta_s/x)$ on the windward plane of symmetry. Free-stream conditions in table 1: ▼, H28; ●, L28; ▲, H22; ◆, L22. (a) normalized against x, the distance from the cone tip and the density ratio, ρ_s/ρ_∞, across a 45° oblique shock with chemistry frozen. (b) Normalized against $\varDelta_f$ and $\varDelta_e$, the frozen and equilibrium limit values of $\varDelta_s$ found by computation for the corresponding free-stream conditions.

We also consider the pitching moment about the cone tip,

$$M_z = \int (p_s - p_\infty)\,\hat{\boldsymbol{k}}\cdot\hat{\boldsymbol{n}}\times r_s\,\mathrm{d}A_s, \tag{20}$$

where $\hat{\boldsymbol{n}}$ is the outward-pointing unit vector normal to an element of the cone surface $\mathrm{d}A_s$, p_s is the pressure acting on that element, r_s is the position vector from the cone tip to the element and $\hat{\boldsymbol{k}}$ is the unit vector along the z-axis. The contributions to the integral in (20) can be separated into those from the windward surface (where $\boldsymbol{u}_\infty\cdot\hat{\boldsymbol{n}} < 0$) and those from the leeward surface (where $\boldsymbol{u}_\infty\cdot\hat{\boldsymbol{n}} > 0$). Figure 10 shows the data for the windward component of the pitching moment coefficient,

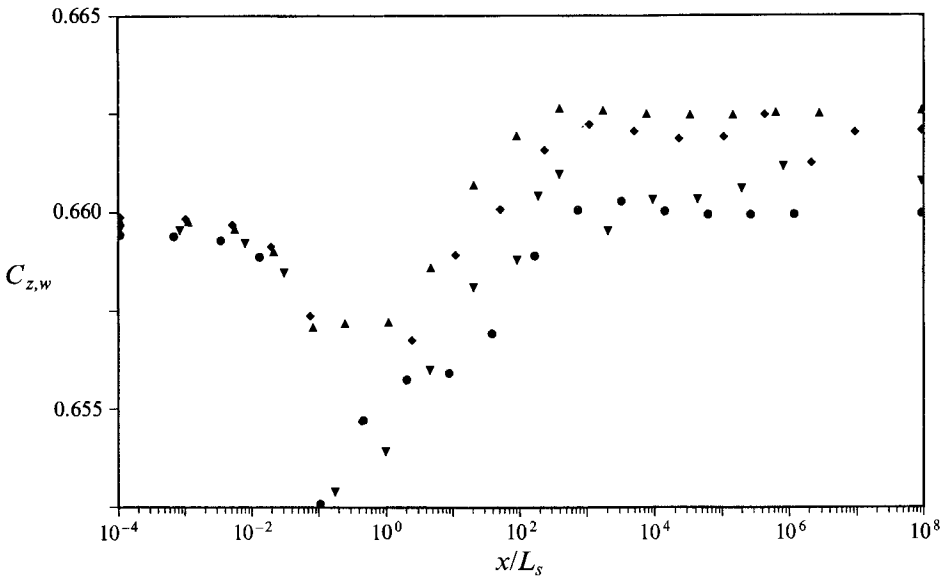$$C_{z,w} = M_{z,w}/(\tfrac{1}{2}\rho_\infty u_\infty^2\,xA_x),$$

FIGURE 10. Integrated pitching moment coefficient, up to the distance x, for windward pressure forces only. Free-stream conditions in table 1: ▼, H28; ●, L28; ▲, H22; ◆, L22.

where $M_{z,w}$ was evaluated from (20) with the area of integration confined to the windward surface of the cone. These data are more scattered than the data for the leeward component, $C_{z,l}$, which are shown later in figure 15, because the cells in the windward portion of the computational grid are larger than in the leeward grid. Nevertheless for each set of free-stream conditions there is sudden change in the behaviour of $C_{z,w}$ at $x/L_s \approx 0.02$, which is the point where the vortex size data indicated that the onset of chemical non-equilibrium occurs. There is a minimum in the pitching moment somewhere in the range $0.1 < x/L_s < 0.4$ followed by an increase to virtually constant values, for $x/L_s > 300$, which are higher than the values found with the chemistry frozen. The relative decline in the pitching moment, as well as the limiting value for equilibrium chemistry, is different in each case. These data again show how the transition from the chemically frozen limit to the chemical equilibrium limit is not a simple one. The pitching moment is important for aerodynamic design and, as has been emphasized by Stalker (1989), consideration of the non-equilibrium nature of the flow is vital.

It appears that the chemical length L_s is an important parameter governing this flow; the maximum non-equilibrium effect, as shown by the windward component of the pitching moment coefficient (and also by the lift and drag coefficients which were not shown) occurs at $x/L_s \sim O(1)$ and the non-equilibrium regime is roughly $0.02 < x/L_s < 300$. In the limit of equilibrium chemistry the four different free-stream conditions considered produced different limiting values of shock stand-off distance and pitching moment.

7. Leeward flow

We consider now the effect of the non-equilibrium reaction rate on the more complicated flow on the leeward surface. Figure 11 shows vortex images for the cases of frozen chemistry, non-equilibrium chemistry, and equilibrium chemistry. These
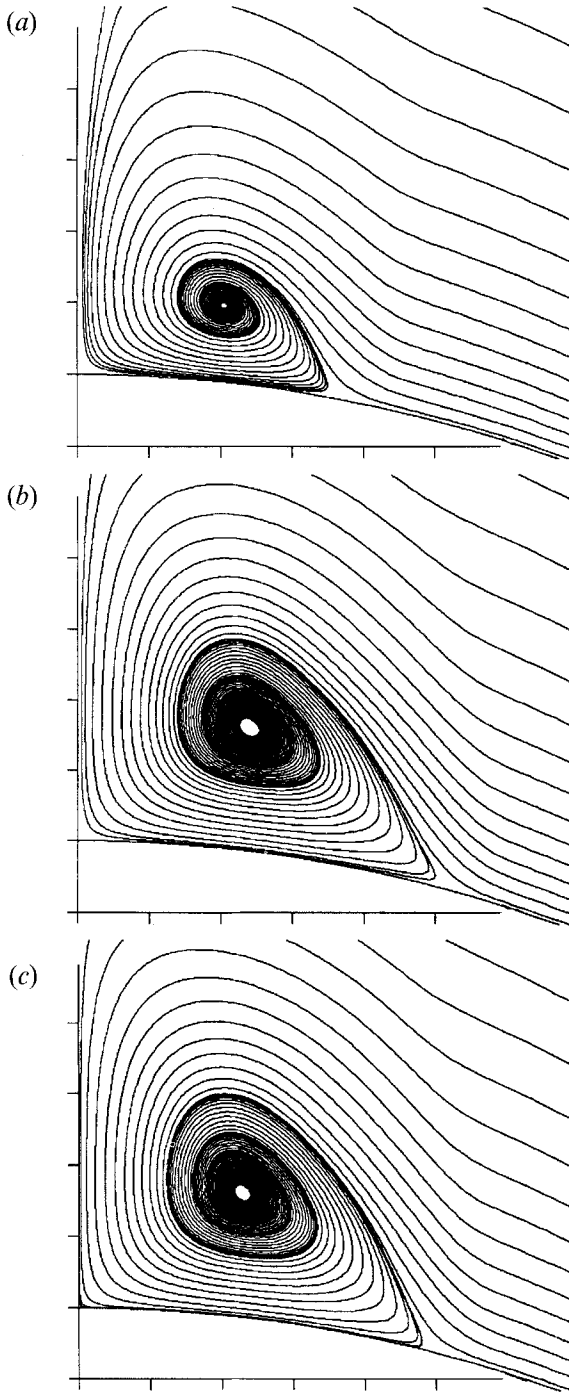
FIGURE 11. Cross-flow vortex: (a) equilibrium chemistry, (b) non-equilibrium chemistry $(x/L_s = 4.25)$, (c) frozen chemistry. Free-stream conditions for case H28 in table 1.

vortex images were all constructed using the same numerical algorithm as that used to produce figure 3. Note that, since the reacting flow is not conically symmetric in this case, the resulting 'streamlines' in a cross-flow section of the grid (which are integral curves of the component of velocity normal to a ray from the cone tip) are not conical
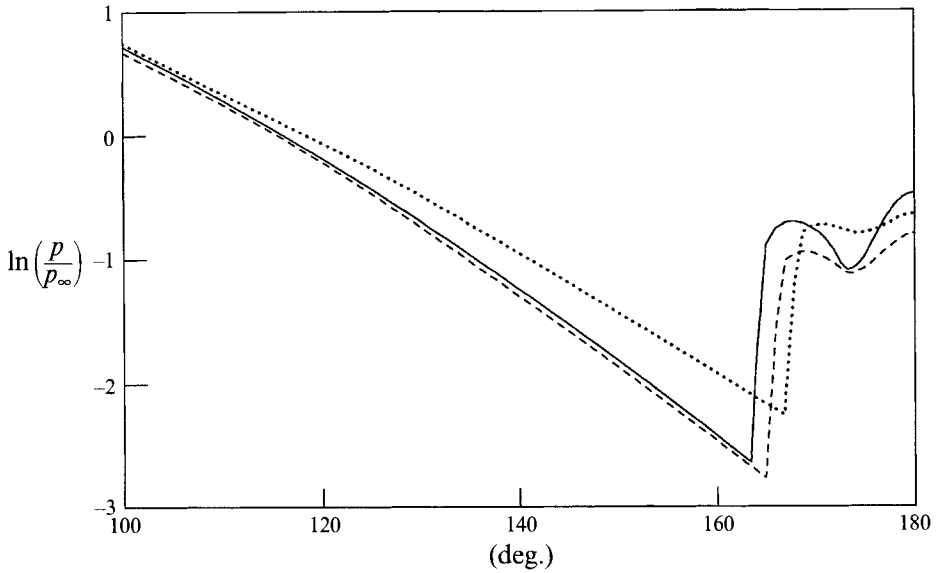
FIGURE 12. Surface pressures for conditions corresponding to figure 11. ———, Frozen; ———, non-equilibrium ($x/L_s = 4.25$); ...., equilibrium chemistry.

projections of stream surfaces. The marked change in the size and aspect ratio of the vortex can be seen for the three cases. Figure 12 shows the surface pressure beneath the vortices shown in figure 11 and here it is clear that the non-equilibrium flow is not simply intermediate between the limiting cases.

The variation in the shock and vortex structure throughout the non-equilibrium regime can be seen in figure 13, which shows contours of the flow Mach number near the leeward plane of symmetry for four different values of x/L_s. The azimuthal location of the cross-flow shock is different at different distances downstream but the shock shape is similar for values of x/L_s of 0.03, 0.89 and 18.8 in the non-equilibrium regime. Far downstream at $x/L_s = 1830$, near the equilibrium limit, the kink in shock shape has almost disappeared and the Mach-number contours roughly follow the streamline shapes in the vortex (see figure 11), which implies that the Mach number varies little as the flow recirculates in the vortex. This is not so for the lower values of x/L_s; there is a local maximum in Mach number at the leeward plane of symmetry and another local maximum at the cone surface. The latter corresponds to the local minimum in pressure seen in figure 12. By reference to figures 11 and 12 it can be seen that as the flow recirculates in the vortex it suffers alternate decreases and increases in Mach number.

The vortex size can be measured by inscribing a rectangle, with sides parallel to the y- and z-axes, around the vortex. All sides of this rectangle can be tangential to the streamline of reversed flow closest to the cone surface which then recirculates and rolls up into the vortex. A convenient measure of the size of the vortex is HW/x^2, where H and W are the height and width, respectively, of the largest possible tangentially inscribed rectangle. The data for vortex size for all computations are shown in figure 14. Values shown at the extreme limits of x are for the frozen and equilibrium calculations. There is a sudden change in behaviour in the data for vortex size at $x/L_s \approx 0.1$ and the data are well collapsed up to $x/L_s \approx 50$. For $x/L_s > 300$ for the high-enthalpy free-stream conditions there appears to be a very slow approach to the
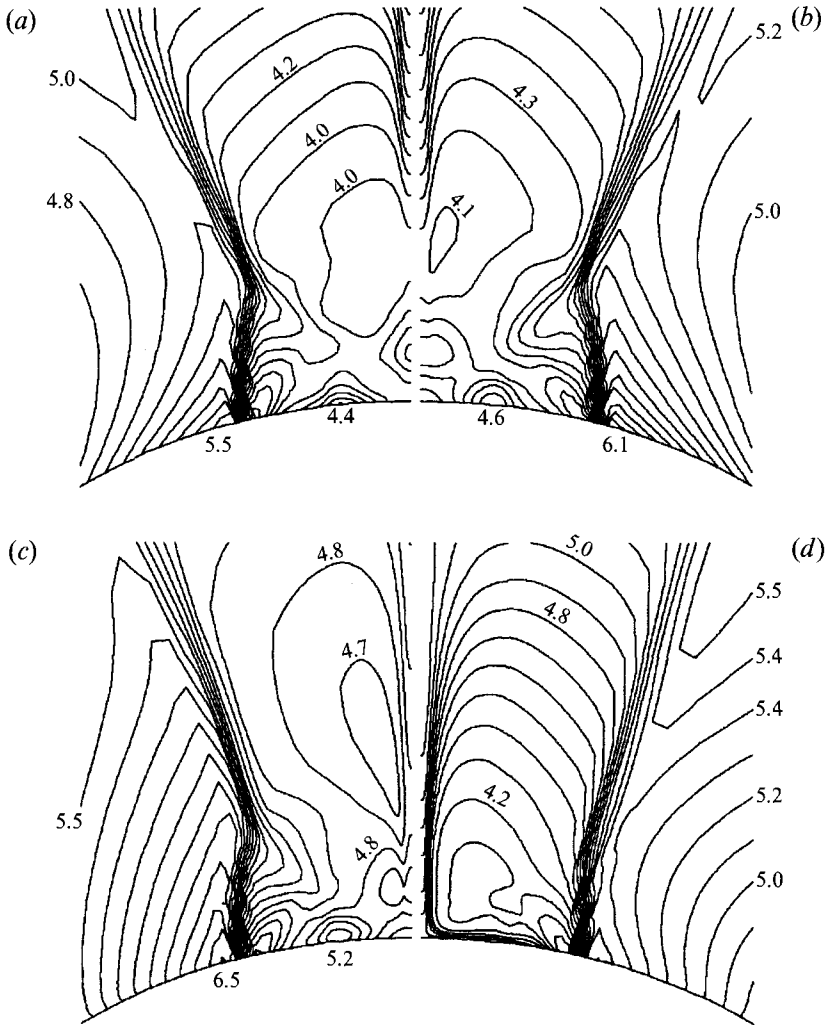
FIGURE 13. Contours of flow Mach number in a cross-flow slice of the grid near the windward plane of symmetry. (a) $x/L_s = 0.03$, (b) $x/L_s = 0.89$, (c) $x/L_s = 18.8$, (d) $x/L_s = 1829.3$. Free-stream conditions for case H28 in table 1.

equilibrium limit. However, for the low-enthalpy data there seems to be an indication of a plateau in the data above the equilibrium limit. There is also some indication of a similar effect in the data shown later in figure 16 (a). Other data, shown in figures 9, 10 and 15, would indicate, despite some scatter, that the calculations have been marched downstream far enough to reach the equilibrium limit. There must remain some doubt about the exact nature of the approach to equilibrium and whether different properties approach the equilibrium limit at significantly different rates. This would seem to be an extremely difficult question to resolve numerically.

Figure 15(a) shows data for $C_{z,l}$, the leeward contribution to the pitching moment coefficient, which is derived from (17) and (20), with integration in (20) confined to the leeward cone surface. The onset of non-equilibrium flow after the upstream frozen flow behaviour is at $x/L_s \approx 0.4$ and there is an immediate separation between the high- and low-energy data. This is followed by a further division of the data at values of $x/L_s \approx 5$ for the low-energy flow and $x/L_s \approx 20$ for the high-energy flow. The data
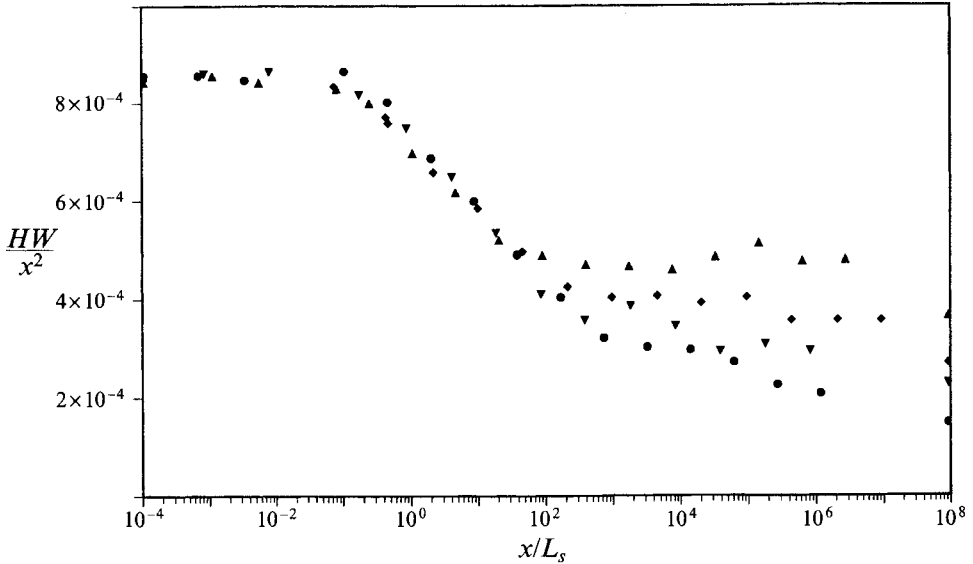
FIGURE 14. Vortex size. Free-stream conditions in table 1: ▼, H28; ●, L28; ▲, H22; ◆, L22.

do not approach the equilibrium limit until $x/L_s > 10^5$. This can be seen more clearly in figure 15(b) which shows a normalized coefficient

$$(C_{z,l} - C_e)/(C_f - C_e)$$

where C_e and C_f are the values of $C_{z,l}$ at the limits of equilibrium and frozen chemistry respectively.

The conclusion from the data for the leeward flow is that the chemical length L_s is a useful normalizing parameter for detecting the onset of chemical non-equilibrium effects, which first become apparent at $x/L_s \approx 0.04$. However, as equilibrium is approached the lengthscale L_s is inadequate to characterize the leeward flow; this is shown particularly by the data for the leeward component of pitching moment in figure 15. What is needed is some measure of how the conditions ahead of the leeward cross-flow shock are affected by the different free-stream conditions and the different lengths of reacting flow traversed by each fluid particle between the windward and leeward shocks. In the next section we use a simple numerical model to estimate the conditions ahead of the leeward shock at any distance from the cone tip. We then use these pre-shock conditions to estimate the conditions behind the cross-flow shock. Finally these post-shock conditions are used to determine an appropriate chemical lengthscale in the leeward flow.

8. Chemical lengthscale in the leeward flow

We can estimate the leeward flow conditions by extending a simple modelling technique developed by Krek *et al.* (1989). The method is to model the (slip) flow along the windward surface of the cone by assuming that the pressure at the surface is everywhere given by the local Newtonian pressure, $\rho_\infty (u_\infty \cdot \hat{n})^2$ for $u_\infty \cdot \hat{n} < 0$, where n is the outward-pointing normal to the cone surface. The velocity at the cone surface is given by the component of the free-stream velocity that is parallel to the surface. These assumptions are enough to determine a set of surface streamlines on the windward surface and to reduce the flow on every streamline to one with a known variation of
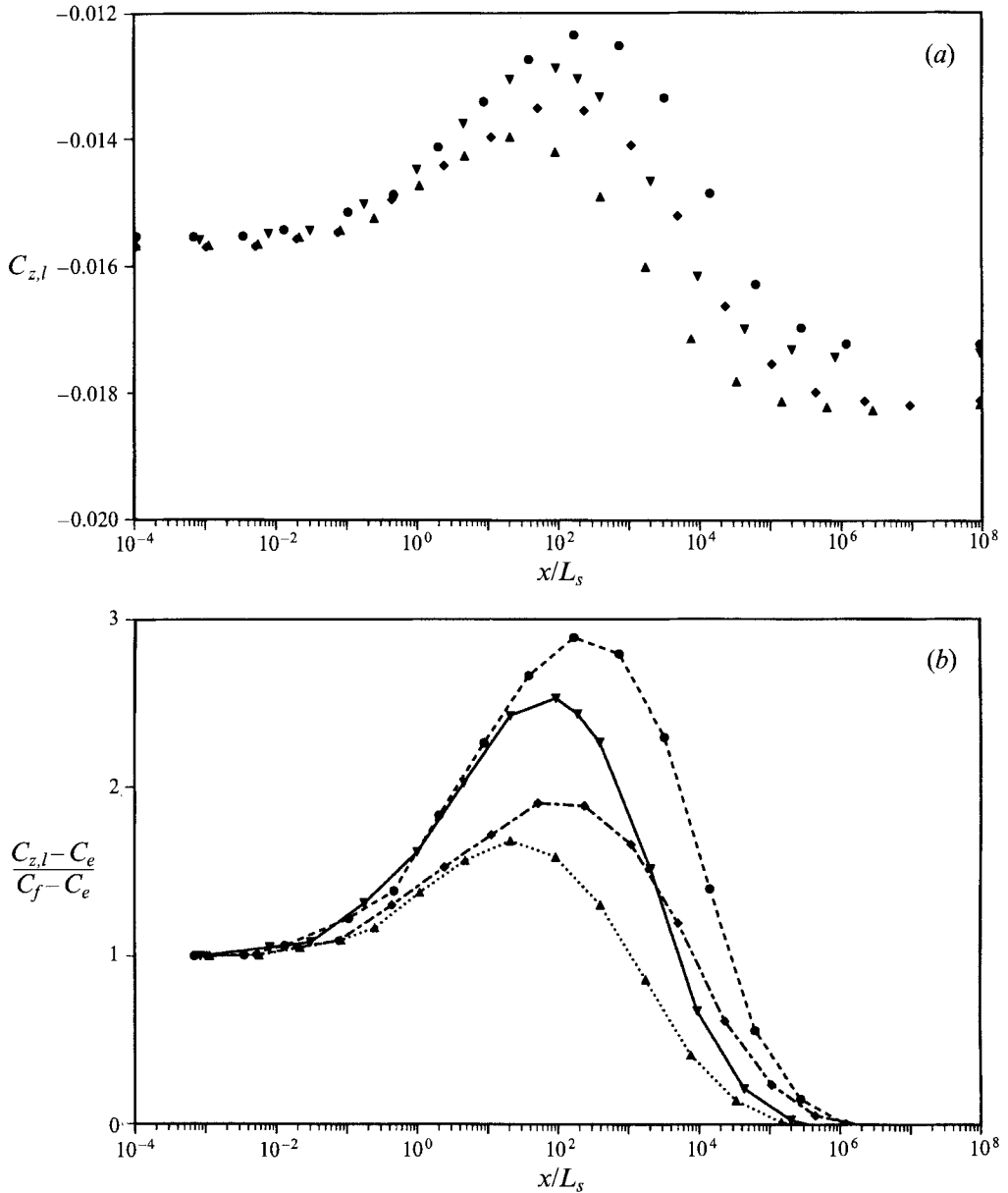
FIGURE 15. (a) Integrated pitching moment coefficient, up to distance x, for leeward pressure forces only. Free-stream conditions in table 1: ▼, H28; ●, L28; ▲, H22; ◆, L22. (b) Normalized pitching moment coefficient. C_f and C_e are the values of $C_{z,l}$ found by computation for the frozen and equilibrium limits and the corresponding free-stream conditions.

pressure and speed along the streamline. The non-equilibrium chemical reactions can be advanced, subject to the pressure and speed constraints, to determine the flow on the windward surface uniquely up to the line separating the windward surface of the cone from the leeward surface. We refer to this line, where $u_\infty \cdot \hat{n} = 0$, as the 'lee line'.

Next we assume that at the lee line the flow is further processed by a cross-flow shock which is normal to the surface and follows the direction of the lee line. The conditions behind this shock, which turns the flow roughly parallel to the leeward plane of
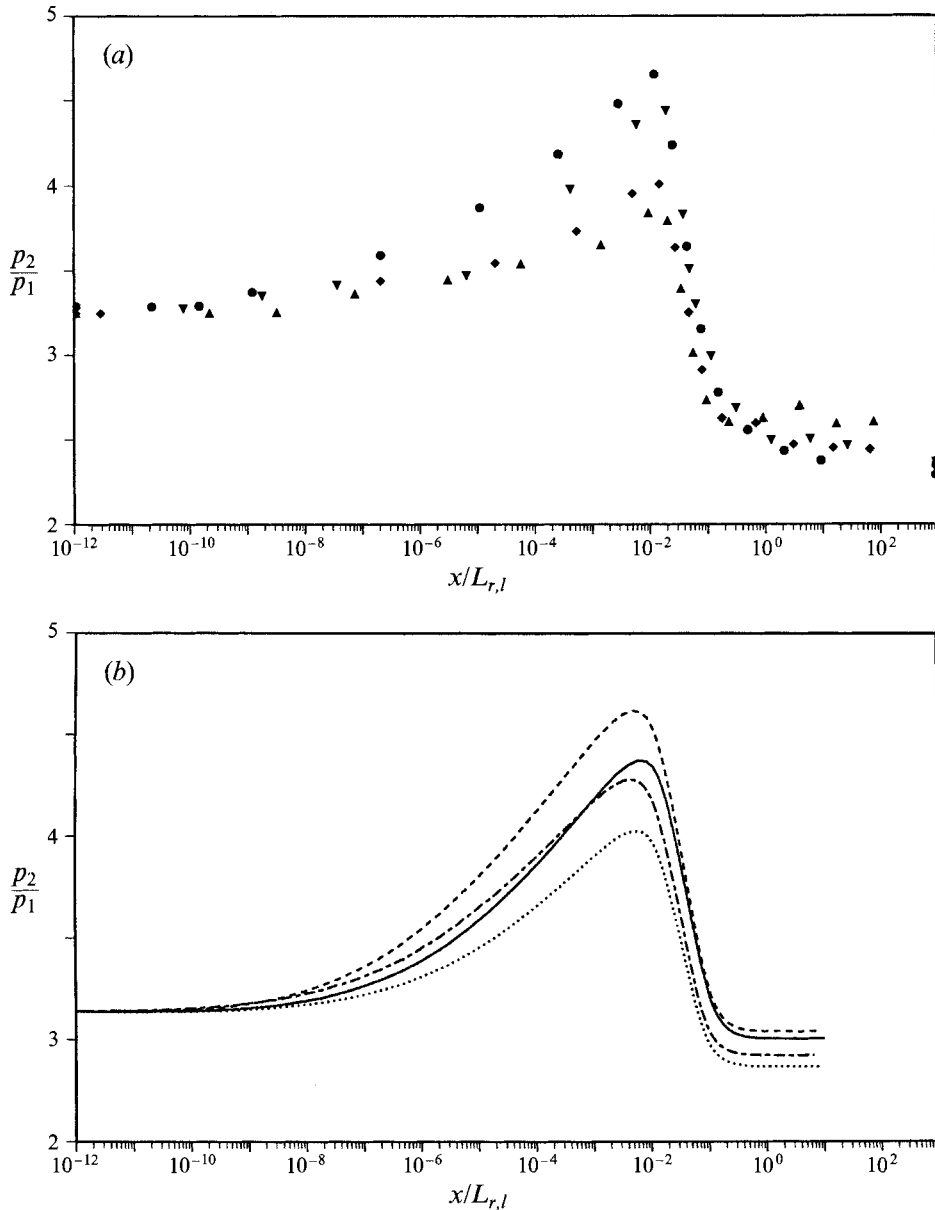
FIGURE 16. Pressure ratio across the leeward shock. $L_{r,l}$ is the chemical length in the leeward flow, (21). (*a*) From three-dimensional EFM calculations, free-stream conditions in table 1: ▼, H28; ●, L28; ▲, H22; ◆, L22. (*b*) From one-dimensional model: ———, H28; ———, L28; ......, H22; ———, L22.

symmetry, can be determined. We have defined a local reaction length for the leeward flow as

$$L_{r,l} = u/(\mathrm{d}\alpha/\mathrm{d}t)_r, \tag{21}$$

where $(\mathrm{d}\alpha/\mathrm{d}t)_r$ is the recombination rate of (9) evaluated for conditions of chemical equilibrium behind the cross-flow shock and u is the predicted magnitude of the post-shock velocity. The chemical equilibrium state has been taken as that resulting from an adiabatic relaxation of the initial frozen chemical state immediately behind the oblique
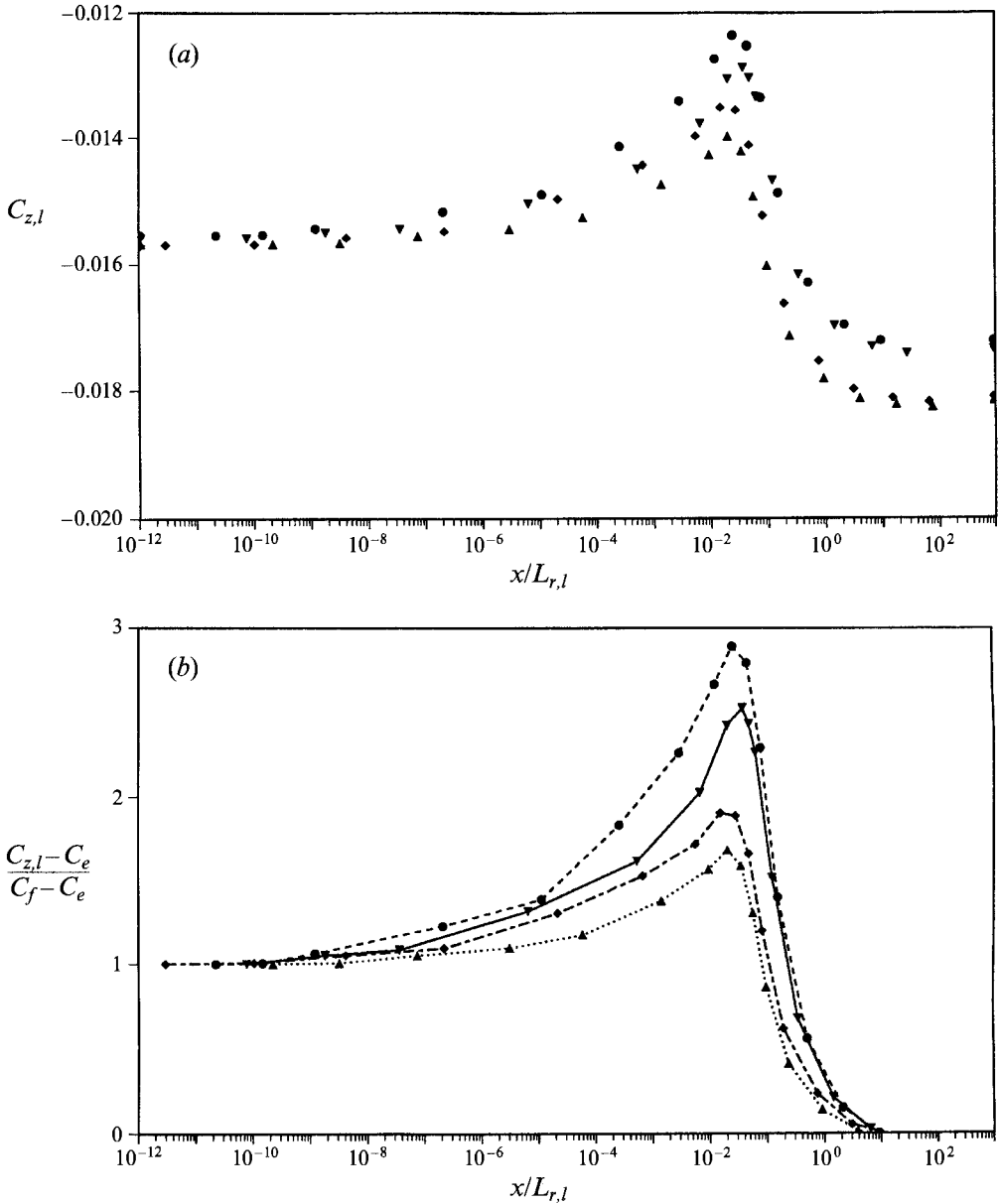
FIGURE 17. Integrated pitching moment coefficient, up to distance x, for leeward pressures forces only. As for figure 15 except that the normalizing length is the recombination length in the leeward flow ($L_{r,l}$ from (21)).

shock, keeping the velocity constant. This lengthscale is a function not only of the free-stream conditions but also of distance from the cone tip. We have determined $L_{r,l}$ numerically for each set of free-stream conditions and for any required distance downstream.

Figure 16(a) shows the pressure ratio across the leeward shock against the distance downstream, normalized as $x/L_{r,l}$ as determined from the EFM calculations. The pre- and post-shock pressures were taken as the minimum surface pressure before the cross-flow shock and the local maximum surface pressure immediately after the shock (see

figure 12). There is a sharp peak in the pressure ratio at $x/L_{r,l} \approx 0.01$ for all free-stream conditions and there is a good collapse of the data in the range $0.01 < x/L_{r,l} < 1$. Figure 16(b) shows the pressure ratio across the 'lee line shock' as predicted by the simple one-dimensional model and the trends in these data are remarkably similar to those in the data from the three-dimensional calculations.

The data for the leeward component of pitching moment, $C_{z,l}$, are shown in figure 17(a) with the distance x normalized against $L_{r,l}$. The collapse of the data is much better than for figure 15 where L_s was used. Here the maximum pitching moment occurs at $x/L_{r,l} \approx 0.01$ and the data for the same stagnation enthalpy but different densities are collapsed. This can be seen more clearly in figure 17(b) where the normalized coefficient

$$(C_{z,l} - C_e)/(C_f - C_e)$$

is shown.

9. Conclusions

The effects of the non-equilibrium nitrogen dissociation reactions on the inviscid flow about a sharp cone at an angle of attack have been investigated. This flow contains a complex shock/vortical structure on the leeward surface. The free-stream conditions considered were similar to those found in a typical high-enthalpy shock-tube wind tunnel. Strong chemical non-equilibrium effects on the aerodynamically important pitching moment coefficient were shown. No simple relations between the non-equilibrium flows and the limiting cases of frozen chemistry and equilibrium chemistry were found.

To some extent the effects of the chemical reactions can be characterized by a single lengthscale, L_s, associated with the reaction rate behind the windward shock. The onset of non-equilibrium effects occurs at $x/L_s \sim O(1)$ for both the windward and leeward flow. The equilibrium limiting values of shock stand-off distance and the windward contribution to the pitching moment are reached at values of x/L_s ranging from 20 to 300. However, the leeward component of the pitching moment displays maximum non-equilibrium behaviour at these values of x/L_s. In the leeward shock/vortical flow the equilibrium limit is not approach closely until values of $x/L_s > 10^5$.

The leeward flow is, in effect, governed by the state of the flow just behind the cross-flow shock. We have extended a simple modelling technique (Krek *et al.* 1989) to predict this state and thus to determine a chemical lengthscale, $L_{r,l}$ governing the leeward flow. That this lengthscale is important in the leeward flow has been shown by the collapse of the leeward pressure data shown in figure 16 and by the improvement in the collapse of the data for the leeward pitching moment coefficient in figure 17 over that given by the use of the lengthscale L_s which is shown in figure 15.

REFERENCES

FREEMAN, N. C. 1958 Non-equilibrium flow of an ideal dissociating gas. *J. Fluid Mech.* **4**, 407.

HORNUNG, H. G. 1972 Non-equilibrium dissociating nitrogen flow over spheres and circular cylinders. *J. Fluid Mech.* **53**, 149.

HORNUNG, H. G. 1976 Non-equilibrium ideal dissociation after a curved shock wave. *J. Fluid Mech.* **74**, 143.

HORNUNG, H. G. 1988 Experimental real-gas hypersonics. *Aero. J.* **92**, 379.

KEWLEY, D. J. & HORNUNG, H. G. 1974 Free-piston shock-tube study of nitrogen dissociation. *Chem. Phys. Lett.* **25**, 531.

KREK, R., HANNEMANN, K., & PULLIN, D. I. 1989 Real gas effects in hypervelocity flows over an inclined cone. In *10 AFMC, University of Melbourne, Paper* 12C-1 (ed. A. E. Perry). University of Melbourne.

LEER, B. VAN 1979 Towards the ultimate conservative difference scheme, Part V. *J. Comput. Phys.* **32**, 101.

LIGHTHILL, M. J. 1957 Dynamics of a dissociating gas. Part 1. Equilibrium flow. *J. Fluid Mech.* **2**, 1.

MACROSSAN, M. N. 1989 The equilibrium flux method for the calculation of flows with non-equilibrium chemical reactions. *J. Comput. Phys.* **80**, 204.

MACROSSAN, M. N. 1990 Hypervelocity flow of dissociating nitrogen downstream of a blunt nose. *J. Fluid Mech.* **217**, 167.

MACROSSAN, M. N. & PULLIN, D. I. 1990 Hypervelocity cone-flow with reaction chemistry by a second order kinetic theory based Euler solver. In *Third Austral. Supercomputer Conf., University of Melbourne December 1990* (ed. K. Sweeny). Strategic Research Foundation, University of Melbourne.

MACROSSAN, M. N., PULLIN, D. I. & RICHTER, N. J. 1989 Calculations of three-dimensional hypervelocity cone-flow with chemical reactions. In *10 AFMC, University of Melbourne, Paper* 12C-3 (ed. A. E. Perry). University of Melbourne.

MARCONI, F. 1989 Complex shock patterns and vortices in inviscid supersonic flows. *Comput. Fluids* **17**, 151.

PULLIN, D. I. 1980 Direct simulation methods for compressible ideal gas flow. *J. Comput. Phys.* **34**, 231.

STALKER, R. J. 1989 Approximations for non-equilibrium hypervelocity aerodynamics. *Ann. Rev. Fluid Mech.* **21**, 37.

YEE, H. C. 1989 A class of high-resolution explicit and implicit shock-capturing methods. *NASA Tech. Mem. 101088.*